Published in final edited form as:

Nat Mater. 2020 May ; 19(5): 559–565. doi:10.1038/s41563-019-0591-1.

Enhanced photocatalytic hydrogen evolution from organic semiconductor heterojunction nanoparticles

Jan Kosco[1,5,*], **Matthew Bidwell**[2,5], **Hyojung Cha**[2], **Tyler Martin**[3], **Calvyn T. Howells**[1], **Michael Sachs**[2], **Dalaver H. Anjum**[1], **Sandra Gonzalez Lopez**[1], **Lingyu Zou**[2], **Andrew Wadsworth**[2], **Weimin Zhang**[1], **Lisheng Zhang**[1], **James Tellam**[4], **Rachid Sougrat**[1], **Frédéric Laquai**[1], **Dean M. DeLongchamp**[3], **James R. Durrant**[2], **Iain McCulloch**[1,2,*]

[1]King Abdullah University of Science and Technology (KAUST), KAUST Solar Center, Physical Sciences and Engineering Division (PSE), Thuwal, Saudi Arabia.

[2]Department of Chemistry and Centre for Plastic Electronics, Imperial College London, London, UK.

[3]Materials Science and Engineering Division, National Institute of Standards and Technology, Gaithersburg, MD, USA.

[4]ISIS, STFC, Rutherford Appleton Laboratory, Chilton, UK.

[5]These authors contributed equally: Jan Kosco, Matthew Bidwell.

Abstract

Photocatalysts formed from a single organic semiconductor typically suffer from inefficient intrinsic charge generation, which leads to low photocatalytic activities. We demonstrate that incorporating a heterojunction between a donor polymer (PTB7-Th) and non-fullerene acceptor (EH-IDTBR) in organic nanoparticles (NPs) can result in hydrogen evolution photocatalysts with greatly enhanced photocatalytic activity. Control of the nanomorphology of these NPs was achieved by varying the stabilizing surfactant employed during NP fabrication, converting it from a core–shell structure to an intermixed donor/acceptor blend and increasing H_2 evolution by an

*Correspondence and requests for materials should be addressed to J.K. or I.M., jan.kosco@kaust.edu.sa; iain.mcculloch@kaust.edu.sa.

Author contributions

J.K. developed the idea, designed and performed experiments, developed analytical tools, analysed data and wrote the paper. M.B. developed the idea, and designed and performed experiments. H.C., T.M., C.T.H. and M.S. designed and performed experiments, and co-wrote manuscript. S.G.L. and W.Z. designed and performed experiments. L.Z. and L.Z. performed experiments. D.H.A. and R.S. imaged nanoparticles. A.W. assisted with manuscript preparation. J.T. assisted with deuteration study. F.L., D.M.D., J.R.D. and I.M. supervised the project.

Online content

Any methods, additional references, Nature Research reporting summaries, source data, extended data, supplementary information, acknowledgements, peer review information; details of author contributions and competing interests; and statements of data and code availability are available at https://doi.org/10.1038/s41563-019-0591-1.

Competing interests

The authors declare no competing interests.

Supplementary information is available for this paper at https://doi.org/10.1038/s41563-019-0591-1.

Data availability

The data shown in the plots, and that support the findings of this study, are available from the corresponding authors on reasonable request.

order of magnitude. The resulting photocatalysts display an unprecedentedly high H_2 evolution rate of over 60,000 μmol h^{-1} g^{-1} under 350 to 800 nm illumination, and external quantum efficiencies over 6% in the region of maximum solar photon flux.

The development of sustainable energy sources is essential to avert impending climate change while sustaining the global population and economic growth[1]. Solar energy is by far the greatest available source of renewable energy, but its transience limits its utility[2]. If solar energy is to provide power on a scale commensurate with or exceeding that currently generated from fossil fuels, it must be stored and supplied to users on demand[2]. Storing solar energy in the chemical bonds of a fuel is therefore highly desirable[2]. H_2 is the simplest such 'solar fuel' and can be generated from water via electrolysis, or using semiconductor photocatalysts that absorb light and convert it to electrical charges that drive surface redox reactions. A 'particulate' system in which photocatalysts are directly dispersed in water is projected to be the cheapest way of producing solar H_2 (ref.[3]). In the simplest case, overall water splitting (OWS) can be achieved by a single photocatalyst that simultaneously oxidizes and reduces H_2O into H_2 and O_2. However, the only particulate photocatalysts currently capable of driving OWS are typically based on single-component, wide bandgap semiconductors, such as TiO_2 (ref.[4]), $SrTiO_3$ (ref.[5]) or carbon nitrides (CN_xH_y)[6,7], which are almost exclusively active at ultraviolet wavelengths, that constitute <5% of the solar spectrum[8]. This fundamentally limits their maximum solar to hydrogen efficiency (η_{STH}) below the target of 10% deemed necessary for commercial viability[3,8]. OWS can also be achieved by two photocatalysts operating in parallel, where the hydrogen evolution reaction (HER) and the oxygen evolution reaction take place on separate semiconductors. This 'Z-scheme' system is analogous to natural photosynthesis, and can potentially achieve higher η_{STH} by employing semiconductors with narrower bandgaps that can absorb a larger proportion of the solar spectrum[9]. Stable, low-cost and efficient O_2 evolution photocatalysts, such as WO_3 (ref.[10]) and $BiVO_4$ (ref.[11]), are active up to 470 and 510 nm, respectively[12], but the development of stable, efficient and low-cost inorganic H_2 evolution photocatalysts (HEPs) has proved more challenging, particularly for HEPs that exhibit complementary absorptions and high activities above 500 nm (refs.[13–15]). This greatly limits the η_{STH} of current Z-schemes and has prompted the recent interest in developing visible light-active HEPs based on organic semiconductors other than CN_xH_y (ref.[7]), whose bandgaps can be tuned to absorb further into the visible spectrum. Conjugated polymers[16,17] and covalent organic frameworks (COFs)[18] have attracted the most attention due to their modular structures, which enable their energy levels and physical properties to be precisely controlled. However, the external quantum efficiencies (EQEs) of these novel non-$(CN)_x$ photocatalysts have been limited by the high exciton binding energies and short exciton diffusion lengths (typically 5–10 nm)[19] of organic semiconductors, which cause high rates of exciton recombination in the semiconductor bulk[20], and hence inefficient generation of charges that can drive redox reactions at the photocatalyst surface. To overcome this limitation, most research has been focused on improving exciton dissociation at the photocatalyst surface by increasing the semiconductor/electrolyte interfacial area via nanoparticle (NP) formation, hydrophilicity enhancements and/or by sensitizing the photocatalyst surface with a suitable dye to create a donor/acceptor (D/A) semiconductor heterojunction that is able to dissociate excitons at the external photocatalyst/dye

interface[21,22]. Less attention has been given to developing organic non-CN_xH_y HEPs with internal semiconductor heterojunctions that can drive exciton dissociation and spatially separate charges in the photocatalyst bulk[17,23]. Conjugated polymer NPs can be readily fabricated with an internal D/A heterojunction by blending donor and acceptor semiconductors together within the same NP[24]. However, this feature has not yet been fully exploited, with most studies to date focusing on optimizing the photocatalytic performance of HEP NPs formed of a single conjugated polymer[25–27].

This work details the development of organic semiconductor NP HEPs that incorporate an internal D/A heterojunction, which enhances exciton dissociation in the NP bulk, leading to greatly enhanced photocatalytic activity compared with single-component NPs. By selecting an appropriate stabilizing surfactant during NP fabrication, it was possible to optimize the heterojunction morphology from the common, but unfavourable, core–shell structure to a more intimately mixed blend, where both donor and acceptor components are present at the NP surface. This dramatically improved the charge extraction from the NPs and resulted in stable (35 h) H_2 evolution photocatalysts with unprecedentedly high activity under broadband visible light illumination, and EQEs exceeding 5% at 660–700 nm. These are amongst the highest EQEs at wavelengths >500 nm reported for any organic HEP to date, and may provide a pathway to high-efficiency solar to chemical energy conversion by substantially improving the η_{STH} of current Z-schemes.

NPs were fabricated via the mini-emulsion process[28], initially employing sodium dodecyl sulfate (SDS) as the stabilizing surfactant, from the donor polymer poly([2,6′−4,8-di(5-ethylhexylthienyl) benzo[1,2-*b*;3,3-*b*]dithiophene]{3-fluoro-2[(2-ethylhexyl)carbonyl]thieno[3,4-*b*]thiophenediyl}) (PTB7-Th) matched with the non-fullerene acceptor EH-IDTBR. The NP size distributions were measured by dynamic light scattering (Supplementary Fig. 1 and Supplementary Table 1). This D/A combination was chosen for its strong visible light absorption (Supplementary Fig. 2), type II energy level offset (Fig. 1) and interfacial morphology, which drives efficient charge separation at the PTB7-Th/EH-IDTBR heterojunction[29] while also generating photoexcited electrons that are sufficiently reducing in the EH-IDTBR lowest unoccupied molecular orbital to drive the HER with the aid of a Pt cocatalyst, as well as sufficiently oxidizing holes in the PTB7-Th highest occupied molecular orbital to oxidize ascorbic acid. Platinum was photodeposited in situ on the organic NP surface during all H_2 evolution measurements. Measuring the HER rates of NPs composed of a range of PTB7-Th:EH-IDTBR mass ratios formed using SDS (Fig. 2a,b) revealed that all D/A NPs formed from a PTB7-Th:EHIDTBR blend were much more active than single-component NPs formed of either pristine PTB7-Th, pristine EH-IDTBR or both pristine NPs mixed together. The HER rate increase is therefore attributed to enhanced charge generation in the blend NPs, driven by their internal D/A heterojunction. This is confirmed by photo-luminescence quenching yield (PLQY) measurements, which show partial quenching of both PTB7-Th and EH-IDTBR excitons for all two-component NP blend compositions (Supplementary Fig. 3). Interestingly, the maximum HER rate ($3{,}044 \pm 332$ μmol h^{-1} g^{-1}) occurred at a blend ratio (EH-IDTBR mass fraction of 90%) where there is insufficient PTB7-Th to efficiently quench all excitons generated in EH-IDTBR, as indicated by the relatively low EH-IDTBR PLQY (52%; Supplementary Fig. 3). We attributed the suppressed HER rates at <90% EH-IDTBR to a core–shell NP

morphology, as indicated by the structural analyses detailed below. This morphology would allow exciton dissociation at the PTB7-Th/EH-IDTBR heterojunction, but would subsequently confine most photogenerated electrons to the EH-IDTBR core, thus preventing efficient electron extraction to the Pt cocatalyst at the NP surface and leading to low photocatalytic activity. Increasing the EH-IDTBR fraction increases the probability of NPs having a partially exposed EH-IDTBR core onto which Pt can be deposited, which improves electron extraction from the NP. This gradually increases the HER rate until the EH-IDTBR mass fraction exceeds a threshold value between 85 and 90%, at which point PTB7-Th can no longer fully encapsulate the EH-IDTBR core, thus allowing more efficient extraction of both electrons from EH-IDTBR and holes from PTB7-Th, and leading to the maximum HER rate at 90% EH-IDTBR.

Core–shell morphologies are common in polymer/small molecule blend nanoparticles prepared from mini-emulsions stabilized by SDS[30–32]. This morphology occurs because, as the organic solvent is removed, the low volatility components phase segregate to minimize interfacial tension between one another and between the continuous and disperse phases of the emulsion[33]. The chloroform/water interfacial tension in the presence of SDS was twice as high when the chloroform phase contained EH-IDTBR versus PTB7-Th (Supplementary Fig. 4). Therefore, when forming NPs from a mixed PTB7-Th/EH-IDTBR solution, it is thermodynamically favourable for PTB7-Th to segregate to the surface of the emulsified chloroform droplets to minimize their surface tension; eventually forming NPs with a PTB7-Th-rich shell and an EH-IDTBR-rich core. We attribute the difference in interfacial tensions to a greater affinity between the long aliphatic tail of SDS and the higher alkyl chain density of PTB7-Th compared with EH-IDTBR. Correspondingly, a surfactant with a short aromatic tail, such as sodium 2-(3-thienyl)ethyloxybutylsulfonate (TEBS)[34] was expected to have increased affinity for EH-IDTBR, because it can interact more strongly with its exposed aromatic units. In the presence of TEBS, the chloroform/water interfacial tensions were almost identical when the chloroform phase contained EH-IDTBR versus PTB7-Th (Supplementary Fig. 4). Because the affinity of TEBS for PTB7-Th and EH-IDTBR is approximately equal, radial segregation of PTB7-Th or EH-IDTBR within the NP is no longer thermodynamically favoured. Consequently, when TEBS is employed as the stabilizing surfactant, PTB7-Th and EH-IDTBR are expected to be more homogeneously mixed throughout the NP and to reside at its surface in approximately equal proportions; providing pathways for efficient extraction of both electrons and holes and thereby increasing the HER rate. Employing TEBS during NP formation dramatically enhanced the HER rates of the blend NPs at all PTB7-Th:EH-IDTBR ratios (Fig. 2b,c), with the maximum HER rate (28,133 ± 3,067 μmol h^{-1} g^{-1}) increasing by almost an order of magnitude compared with NPs formed using SDS. The optimum blend composition also shifted from an EH-IDTBR mass fraction of 90% to one of 70%; a composition in which there is more efficient exciton dissociation, as evidenced by PL quenching (Supplementary Fig. 3), and which has been previously reported to deliver optimal photon conversion efficiency in the active layer of solar cells[35]. An even greater increase in the relative HER rate on replacing SDS with TEBS as the stabilizing surfactant was observed for P3HT:PCBM NPs (Supplementary Fig. 5), which highlights the broad applicability of this

technique for optimizing the morphology of D/A NP photocatalysts formed from a wide range of solution-processable semiconducting polymers and small molecules.

To confirm that the increased HER rates in NPs formed using TEBS were indeed due to a transition from a core–shell to an intermixed NP morphology, the internal morphologies of PTB7-Th/EH-IDTBR NPs fabricated using TEBS and SDS were analysed by cryo-transmission electron microscopy (cryo-TEM, Fig. 3). This technique was chosen because it can image the NPs in an environment that is close to their native state, and therefore sample preparation is expected to preserve their morphology. Single-component PTB7-Th NPs formed using SDS or TEBS (Fig. 3a,b) are both amorphous, as indicated by the round NP shape and relatively featureless nanoparticle projection, which suggests that there is little structural order in the polymer microstructure. Single-component EH-IDTBR NPs formed using SDS and TEBS (Fig. 3c,d) both had highly crystalline structures with a lattice spacing of 1.6 nm, which was clearly visible as lines of alternating high and low electron density. This spacing is consistent with the diffraction peak at 0.39 $Å^{-1}$ in the grazing incidence X-ray diffraction (GIXRD) pattern of an annealed EH-IDTBR thin film[36]. However, EH-IDTBR NPs formed using SDS mostly consisted of a single EH-IDTBR crystal, as indicated by the hexagonal nanoparticle projection and the constant lattice orientation throughout the NP, whereas EH-IDTBR NPs formed using TEBS had a more polycrystalline structure with multiple lattice orientations and visible grain boundaries. The polycrystallinity is attributed to the higher chloroform/water interfacial tension in the presence of TEBS versus SDS (Supplementary Fig. 4). This induces more rapid EH-IDTBR nucleation and hence a more polycrystalline NP structure. Two-component PTB7-Th/EH-IDTBR particles formed using SDS typically exhibit a crystalline phase in the particle core surrounded by a thin amorphous shell. The lattice spacing of the crystalline domain is close to that observed in pure EH-IDTBR (1.7 nm), and the lattice planes have the same orientation throughout the crystalline domain, which suggests that the particle core is formed from a single EH-IDTBR crystal. In a 95-nm diameter particle shown in Fig. 3e, the crystalline core radius is approximately 42 nm and the amorphous shell radius is approximately 5 nm. Modelling the particle as a sphere, and assuming equal densities of PTB7-Th and EH-IDTBR (Supplementary Fig. 7), shows that the volume of the core and shell domains is consistent with the 30:70 PTB7-Th:EH-IDTBR mass ratio in the blend. Furthermore, the 30:70 PTB7-Th:EH-IDTBR NPs formed using SDS occasionally display an additional periodic spacing in the shell (2.14 nm; see Fig. 5a), which corresponds to the lamellar stacking distance of PTB7-Th determined by GIXRD[37]. Both these observations strongly suggest that the NPs formed using SDS are composed of a crystalline EH-IDTBR core surrounded by an amorphous PTB7-Th shell, which is in agreement with the interfacial tensions measured in the presence of SDS (Supplementary Fig. 4), as well as the trend in HER rate with blend composition (Fig. 2a,b). Two-component PTB7-Th/EH-IDTBR NPs formed using TEBS comprise a distributed blend of crystalline and amorphous domains. The crystalline domains showed two different lattice spacings, 1.9 nm and 3.2 nm, both of which correspond to minor peaks in the GIXRD pattern of an EH-IDTBR film at Q=0.33 $Å^{-1}$ and 0.19 $Å^{-1}$, respectively[36]. This suggests that the rapid crystallization invoked by TEBS can give rise to multiple EH-IDTBR polymorphs forming within the NP, as has been previously observed in P3HT/EH-IDTBR blend films[38]. Therefore, on the basis of the 30:70 mass ratio of PTB7-Th and EH-IDTBR

within the NP, the crystalline regions with 1.9- and 3.2-nm lattice spacings are both assigned to EH-IDTBR. The lack of any apparent radial segregation between the PTB7-Th and EH-IDTBR within the NP, and an approximately equal distribution of PTB7-Th and EH-IDTBR at the NP surface, is consistent with the interfacial tensions measured in the presence of TEBS (Supplementary Fig. 4) as well the dramatically increased HER rates achieved with NPs formed using TEBS versus SDS.

Small-angle neutron scattering (SANS) (Fig. 4) of blend NPs of PTB7-Th and deuterated EH-IDTBR (dEH-IDTBR) in D_2O/H_2O solutions further supports the morphological analysis from the cryo-TEM. In Fig. 4a, NPs formed using SDS surfactant near the contrast match point of PTB7-Th (volume fraction of 24.7% D_2O) indicate a spherical dEH-IDTBR core. At contrasting conditions near those of dEH-IDTBR (volume fraction of 82.0% D_2O), a large feature emerges at a middle q range of $0.02 < q < 0.2$ Å^{-1}. Despite the visual appearance of the NPs in Fig. 3e, no core–shell model could be fit to the full range of data shown. This includes core–shell models with varying number of shell layers and varying mathematical descriptions of the layer interfaces. To further understand the data, we decomposed the contrast series into partial scattering functions (Fig. 4c), which isolate the contributions from the PTB7-Th ($S_{PTB7-Th}(q)$) and dEH-IDTBR $S_{dEH-IDTBR}(q)$) to the total scattering function, $\frac{d\Sigma}{d\Omega}(q)$ (ref.[39]), which represents the scattered neutron intensity on an absolute scale with $d\Sigma$ being a differential scattering cross section and $d\Omega$ the differential solid angle of scattering. This analysis clearly shows that the mid-q feature arises from the PTB7-Th domain, while the dEH-IDTBR scattering is described well by a spherical form factor model. Taken together, these data describe the particle as having a spherical dEH-IDTBR core and a PTB7-Th domain(s) that displays a broad secondary length scale. Given the cryo-TEM analysis, this secondary length scale probably still describes a shell-like feature, but there is some additional structural complexity that is not captured in the core–shell models explored here (for example, local aggregation of PTB7-Th on the core surface, or PTB7-Th/SDS mixed morphologies). The NPs formed using TEBS also showed no substantial secondary length scale at any SANS contrast condition (Fig. 4b). Simultaneous fits to the spherical form factor model with the radius (R) and log-normal dispersity $\left(\frac{dR}{R}\right)$ parameters constrained across contrasting conditions yields reasonable fits (R = 10:2 nm; $\frac{dR}{R} = 0.57$). The decomposed partial scattering functions (Fig. 4c) also show spherical behaviour, with $S_{dEH-IDTBR}(q)$ displaying a better fit than $S_{PTB7-Th}(q)$. The deviations in $S_{PTB7-Th}(q)$, along with those of the full scattering curves at intermediate contrast conditions (Fig. 4b), indicate that there is microstructure that is not perfectly described by a spherical model. These observations are probably related to the multiple amorphous and crystalline domains observed in the cryo-TEM (Fig. 3f). Overall, the SANS analysis indicates that the blend NPs prepared with TEBS are more intermixed than their SDS counterparts, which is consistent with the transition from a core–shell NP morphology to a more intermixed D/A heterojunction NP. This is further supported by Kelvin probe force microscopy (Supplementary Fig. 12), which shows that the work function of the blend NPs formed with TEBS is greater than that of those formed with SDS; suggesting a more EH-IDTBR-rich surface in the TEBS-formed NPs.

The photodeposited Pt cocatalyst decorates the surface of the PTB7-Th/EH-IDTBR NPs (Fig. 5) and facilitates electron transfer from the photocatalyst to protons in the aqueous phase by providing sites for proton adsorption and electron accumulation[26,40]. Optimizing the Pt loading further increased the HER rate of the best-performing NPs (30:70 mass ratio PTB7-Th:EH-IDTBR TEBS) to a maximum of 64,426 ± 7,022 μmol h^{-1} g^{-1} at 10% Pt (Supplementary Fig. 14). This is one of the highest mass-normalized HER rates reported to date for an organic HEP under broadband visible light irradiation[7,21,41]. Measuring the EQEs of the NPs over a range of wavelengths (Fig. 6a) revealed that the NPs were highly active throughout the visible spectrum, achieving EQEs of 2.0%, 2.3%, 4.3%, 5.6% and 6.2% at 400, 500, 620, 660 and 700 nm, respectively. This is in contrast to state-of-the-art CN_xH_y HEPs, which can achieve higher EQEs at wavelengths <450 nm but are inactive above 500 nm due to their wide bandgaps[7]. High EQEs at wavelengths >500 nm are essential for the photocatalyst to efficiently utilize photons in the region of maximum solar photon flux, and hence achieve high η_{STH} (ref.[8]). The EQEs of the PTB7-Th/EH-IDTBR NPs at wavelengths ≥500 nm are substantially higher than those reported for any organic HEP[7,21,41], and make the PTB7-Th/EH-IDTBR HEPs particularly attractive for use in a Z-scheme, in conjunction with an efficient wide bandgap O_2 evolution photocatalyst, such as WO_3 (ref.[10]) or $BiVO_4$ (ref.[11]), that is only active at wavelengths <500 nm.

The HER rate of the optimized PTB7-Th:EH-IDTBR NP photocatalysts was compared to a range of benchmark materials measured in the same reactor, under illumination from the same light source (Fig. 6b,c). To ensure a fair comparison between photocatalysts, the HER rates were measured under saturated conditions (0% light transmission through the reactor throughout the absorption range of the photocatalyst)[42]. The Pt loadings of CN_xH_y(1%)[43], TiO_2 (1.5%)[44] and poly(9,9-dioctylfluorene-*alt*-benzothiadiazole) (F8BT) (5%)[26] were chosen on the basis of previously reported optima, and the photocatalytic activities reported for CN_xH_y and TiO_2 are the higher of two measurements taken in the presence of different sacrificial reagents (ascorbic acid or triethanolamine). HER rates were compared in terms of the absolute amount of H_2 produced per hour[45]. The average HER rate over 16 h for the PTB7-Th/EH-IDTBR NP photocatalysts (128.9 μmol h^{-1}) was over 4 times higher than that of TiO_2 (32.1 μmol h^{-1}), almost 10 times higher than that of commercial CN_xH_y (13.3 μmol h^{-1}) and over 75 times higher than F8BT NPs (1.7 μmol h^{-1}), a commonly studied single-component conjugated polymer photocatalyst[26,46]. Although the optimum Pt loading (10%) was higher for the PTB7-Th/EH-IDTBR NPs than for the other photocatalysts, when comparing photocatalytic activities in terms of HER rate per total mass of Pt used (Fig. 6d), the activity of the PTB7-Th/EH-IDTBR NPs rises even further above the CN_xH_y and TiO_2 benchmarks. This is because the strong light absorption and efficient charge generation of the PTB7-Th/EH-IDTBR NPs allows them to produce more photogenerated charges per unit mass of photocatalyst. This increases the turnover frequency of the Pt cocatalyst (Supplementary Table 3) compared with the benchmark photocatalysts, which is highly advantageous in terms of both cost and scalability[47].

We have demonstrated the fabrication of organic NP HEPs with an internal D/A semiconductor heterojunction, which greatly improves charge generation inside the NP bulk, and thus greatly enhances photocatalytic activity compared with NPs formed from a single organic semiconductor. By varying the stabilizing surfactant employed during NP

fabrication it was possible to optimize the heterojunction morphology from an unfavourable core–shell structure to a more intimately mixed blend. This improved charge extraction from the NPs and increased the HER rate of PTB7-Th/EH-IDTBR NPs by almost an order of magnitude, leading to the unprecedentedly high HER rate of 64,426 ± 7,022 μmol h^{-1} g^{-1} under broadband visible light illumination, high photocatalytic activity throughout the visible spectrum and EQEs exceeding 5% at 660 to 700 nm. The EQEs at wavelengths >500 nm are amongst the highest reported for an organic HEP to date, and may provide a pathway to increased η_{STH} for current Z-schemes via improved visible light utilization. Furthermore, the NP fabrication and heterojunction optimization process provides a platform for the vast library of existing soluble organic semiconductors to be processed into NP photocatalysts that are energetically tailored to drive a wide range of redox chemistries, including OWS, CO_2 reduction[48] and N_2 fixation[49], which all rely on the same fundamental photon-to-electron conversion processes as photocatalytic hydrogen evolution.

Methods

Nanoparticle fabrication.

Individual stock solutions (0.50 mg ml^{-1}) of PTB7-Th and EH-IDTBR were prepared in chloroform. The solutions were heated overnight (80 °C) to ensure complete dissolution and filtered (0.2-μm PTFE). Nanoparticle precursor solutions were prepared from the stock solutions by mixing them in the ratio of the desired nanoparticle composition. Nanoparticle precursor solution (5 ml) was then added to a 0.5 wt% solution of surfactant (SDS or TEBS) in water (10 ml) and stirred vigorously for 15 min at 40 °C to form a pre-emulsion, which was then sonicated for 5 min with an ultrasonic processor (Sonics VibraCell VCX130PB) to form a mini-emulsion. The mini-emulsion was heated at 85 °C under a stream of air to remove the chloroform, leaving a surfactant-stabilized nanoparticle dispersion in water. Finally, the dispersion was filtered (0.45-μm glass fibre) to remove any large aggregates or debris from the processor tip.

Dynamic light scattering.

The size distribution of each nanoparticle batch was measured by dynamic light scattering (Malvern Zetasizer ZS; Supplementary Fig. 1 and Supplementary Table 1). Supplementary Fig. 1 shows that all NP batches had unimodal size distributions and that the Z_{avg} hydrodynamic diameter between batches remained relatively constant at 50–80 nm, regardless of whether SDS or TEBS was used as the stabilizing surfactant. TEBS narrowed the NP size distributions and slightly increased the Z_{avg} NP size for all PTB7-TH:EH-IDTBR ratios, but, overall, all NP batches were of a similar size. This is important when comparing HER rates between batches because NP size affects the total available surface area, which would probably affect the HER rate. Having samples with similar size distributions minimizes this variation and allows the effects of nanoparticle composition and morphology to be isolated.

Cryo-TEM.

Cryo-TEM of the samples was carried out with a Titan Krios 80–300 TEM (ThermoFisher Scientific). This microscope is optimized for carrying out cryo-TEM analysis of liquid

samples. It is also equipped with an energy filter model GIF Quantum 968 (Gatan) underneath the column to filter the energy-loss electrons to improve the contrast in the acquired images. Moreover, behind the GIF column, a highly sensitive direct electron complementary metal oxide semiconductor camera of (model K2, Gatan) was installed for recording high-resolution images at extremely low electron dose conditions (~1 e^{-} $Å^{-2}$). Specimen preparation of samples for cryo-TEM analysis was carried out by using an automated plunge-freezing tool (Vitrobot Mark-IV). Moreover, the specimens were prepared with a special type of copper TEM grid (Quatifoil MultiA). These grids have a carbon layer with various sizes of holes and were chosen with the purpose of varying the ice thickness in the holes. In this way, the chance of organic particles being present in the specimen was dramatically higher than with the single hole-size carbon containing grid. Each specimen was prepared by placing 3.5 μl of solution onto the grids followed by 1 s of blotting time and plunge freezing into liquid ethane cryogen. The cryo-TEM analysis was performed by setting the microscope at an acceleration voltage of 300 kV. Before the analysis, the microscope as well as the GIF column were aligned to achieve higher quality images. Furthermore, the images were recorded under so-called dose-fractionation conditions. In fact, instead of acquiring a single frame with total electron beam exposure time, the images were acquired in stacks that contained frames whose exposure time was more than ten times smaller than the total exposure time. The acquired stacks were then aligned and summed along the *z* direction to give the final images. This method of image recording ensured higher quality images of organic particles with as little damage as possible. The total electron dose given to images acquired at low magnifications (<50,000 times) was kept below 10 e^{-} $Å^{-2}$, whereas higher magnification images (>100,000 times) received an electron dose of about 20 e^{-} $Å^{-2}$, so as to maintain good signal-to-noise conditions. It should be noted that the entire image acquisition, as well as the processing, was performed using Gatan Microscopy Suite v.3.2.

Hydrogen evolution.

Hydrogen evolution from PTB7-TH/EH-IDTBR nanoparticles was measured using ascorbic acid as a sacrificial electron donor. PTB7-TH/EH-IDTBR nanoparticles with varying PTB7-TH:EH-IDTBR ratios (2 mg) in 0.2 M ascorbic acid (20 ml) were loaded into a recirculating batch reactor (area, 452 mm^2), which has been previously reported[42]. The desired Pt loading was achieved by adding a specific amount of aqueous potassium hexachloroplatinate solution (0.401 mg ml^{-1} Pt). The reactor was evacuated and purged with argon five times to remove oxygen, and the pressure was set to 100 Torr. The suspension was stirred and illuminated with a 300-W Xe lamp (Asahi Max 303) fitted with an ultraviolet–visible mirror module (350–800 nm) and H_2 evolution was quantified by a gas chromatograph equipped with a thermal conductivity detector. The same method was used to measure H_2 evolution from TiO_2 and CN_xH_y, except in this case 100 mg of photocatalyst was used and the reaction was carried out either in 0.2 M ascorbic acid or 10 vol% triethanolamine.

EQE measurements.

EQE measurements were carried out in the same way as hydrogen evolution measurements, but with suitable band pass filters fitted to the light source. The sample was first illuminated under unfiltered light (350–800 nm) for 4 h to complete Pt photodeposition. Then, the

reactor was evacuated and purged with argon five times to remove all of the H_2 evolved during this time. The light source was fitted with a band pass filter, and illuminated with filtered light within a narrow wavelength range (irradiance spectra in Supplementary Fig. 16). The EQE was calculated using equation (1), where $n\mathrm{H}_2$ represents the number of moles of H_2 evolved per hour, and n photons represents the total number of photons incident on the reactor per hour. Photon flux was measured using a calibrated spectrometer (Ocean Optics USB2000 calibrated with an Ocean Optics DH3-plus light source) fitted with a fibre optic cable and a 0.4778-cm^2 cosine corrector.

$$\mathrm{EQE}(\%) = \frac{200n\,\mathrm{H}_2}{n\,\mathrm{photons}} \tag{1}$$

Atomic force microscopy.

Nanoparticles were drop-cast on indium tin oxide (ITO)-coated glass substrates and characterized with a Solver Next sample-positioning microscope (NT-MDT) using an atomic force microscopy measuring head. To confirm the core–shell morphology, samples were placed in a plasma asher (HPT-100, Henniker plasma) for two 10-s periods, and a few nanometres of material was removed from the surface of the nanoparticles. Topography and surface potential were measured in semi-contact mode using a 20-nm PtIr-coated conductive 0.01–0.025 ohm cm antimony (n)-doped Si cantilever (SCM-PIT, Veeco). The cantilever had a resonant frequency and stiffness of 60–100 kHz and 1–5 N m^{-1}, respectively. The work function of the tip was estimated by measuring the contact potential difference (V_{CPD}) of a gold standard (5.1 eV) from Digital Instruments Veeco Metrology Group and using the equation:

$$V_{\mathrm{CPD}} = \frac{\phi_{\mathrm{tip}} - \phi_{\mathrm{sample}}}{-e} \tag{2}$$

where ϕ is the work function and e the charge of an electron. The work function of the tip was found to be 5.05 eV (mean V_{CPD} for gold is 50 mV, from Supplementary Fig. 12e). To confirm, a commercial ITO sample was measured (Supplementary Fig. 12f) and the work function estimated as 4.84 eV (mean V_{CPD} for ITO is −213 mV).

Surface and interfacial tension measurements.

Surface and interfacial tensions were measured with a Kruss Tensiometer using the ring method. The probe was rinsed in water and heated until it was red hot. The glass vessel used to hold the liquid was cleaned with acetone and rinsed with water. To confirm no contamination, before each measurement, the surface tension of water was measured. The liquid to be measured was placed in the glass vessel, and the temperature allowed to equilibrate for 30 min. The concentration of TEBS or SDS in deionized water was 0.5 wt% and for PTB7-TH or EH-IDTBR 0.5 mg ml^{-1} in chloroform. The measurements were performed by attaching the probe to a balance. The glass vessel containing the liquid to be measured was raised until it was in contact with the probe.

The sample was then lowered until a maximum force (F_{max}) was recorded. The surface or interfacial tension was calculated according to equation (3).

$$\sigma = \frac{F_{max} - F_v}{L\cos\theta} \quad (3)$$

where F_v is the weight of liquid volume, L the wetted length and θ the contact angle. The contact angle $\theta = 0$ because the force vector is parallel to the direction of motion. A Harkins and Jordan correction factor is applied to correct for the curvature of the film being greater on the inside than on the outside of the ring. The results are shown in Supplementary Fig. 4.

Supplementary Material

Refer to Web version on PubMed Central for supplementary material.

Acknowledgements

The research reported in this publication was supported by funding from King Abdullah University of Science and Technology Office of Sponsored Research (OSR) under awards no. OSR-2018-CARF/CCF-3079 and no. OSR-2015-CRG4-2572. This work was supported by the nSoft consortium. Certain commercial products or company names are identified here to describe our study adequately. Such identification is not intended to imply recommendation or endorsement by the National Institute of Standards and Technology, nor is it intended to imply that the products or names identified are necessarily the best available for the purpose.

References

1. Hoffert MI et al. Advanced technology paths to global climate stability: energy for a greenhouse planet. Science 298, 981–987 (2002). [PubMed: 12411695]
2. Creutzig F et al. The underestimated potential of solar energy to mitigate climate change. Nat. Energy 2, 17140 (2017).
3. Pinaud BA et al. Technical and economic feasibility of centralized facilities for solar hydrogen production via photocatalysis and photoelectrochemistry. Energy Environ. Sci 6, 1983–2002 (2013).
4. Fujishima A & Honda K Electrochemical photolysis of water at a semiconductor electrode. Nature 238, 37–38 (1972). [PubMed: 12635268]
5. Goto Y et al. A particulate photocatalyst water-splitting panel for large-scale solar hydrogen generation. Joule 2, 509–520 (2018).
6. Wang X et al. A metal-free polymeric photocatalyst for hydrogen production from water under visible light. Nat. Mater 8, 76–80 (2009). [PubMed: 18997776]
7. Zhang G et al. Ionothermal synthesis of triazine-heptazine-based copolymers with apparent quantum yields of 60% at 420 nm for solar hydrogen production from “sea water”. Angew. Chem. Int. Ed. Engl 57, 9372–9376 (2018). [PubMed: 29852539]
8. Maeda K & Domen K Photocatalytic water splitting: recent progress and future challenges. J. Phys. Chem. Lett 1, 2655–2661 (2010).
9. Wang Y et al. Mimicking natural photosynthesis: solar to renewable H_2 fuel synthesis by Z-scheme water splitting systems. Chem. Rev 118, 5201–5241 (2018). [PubMed: 29676566]
10. Bamwenda GR & Arakawa H The visible light induced photocatalytic activity of tungsten trioxide powders. Appl. Catal. A 210, 181–191 (2001).
11. Zhu M, Sun Z, Fujitsuka M & Majima T Z-Scheme photocatalytic water splitting on a 2D heterostructure of black phosphorus/bismuth vanadate using visible light. Angew. Chem. Int. Ed. Engl 57, 2160–2164 (2018). [PubMed: 29276822]
12. Kim JH & Lee JS Elaborately modified $BiVO_4$ photoanodes for solar water splitting. Adv. Mater 31, 1806938 (2019).

13. Zhang P, Zhang J & Gong J Tantalum-based semiconductors for solar water splitting. Chem. Soc. Rev 43, 4395–4422 (2014). [PubMed: 24668282]
14. Yuan Y-J, Chen D, Yu Z-T & Zou Z-G Cadmium sulfide-based nanomaterials for photocatalytic hydrogen production. J. Mater. Chem. A 6, 11606–11630 (2018).
15. Zhu X et al. Black phosphorus revisited: a missing metal-free elemental photocatalyst for visible light hydrogen evolution. Adv. Mater 29, 1605776 (2017).
16. Sachs M et al. Understanding structure–activity relationships in linear polymer photocatalysts for hydrogen evolution. Nat. Commun 9, 4968 (2018). [PubMed: 30470759]
17. Zhang X et al. Biomass nanomicelles assist conjugated polymers/Pt cocatalysts to achieve high photocatalytic hydrogen evolution. ACS Sustain. Chem. Eng 7, 4128–4135 (2019).
18. Banerjee T & Lotsch BV The wetter the better. Nat. Chem 10, 1175–1177 (2018). [PubMed: 30464321]
19. Mikhnenko OV, Blom PWM & Nguyen T-Q Exciton diffusion in organic semiconductors. Energy Environ. Sci 8, 1867–1888 (2015).
20. Sun C et al. Interface design for high-efficiency non-fullerene polymer solar cells. Energy Environ. Sci 10, 1784–1791 (2017).
21. Wang X et al. Sulfone-containing covalent organic frameworks for photocatalytic hydrogen evolution from water. Nat. Chem 10, 1180–1189 (2018). [PubMed: 30275507]
22. Takanabe K et al. Photocatalytic hydrogen evolution on dye-sensitized mesoporous carbon nitride photocatalyst with magnesium phthalocyanine. Phys. Chem. Chem. Phys 12, 13020–13025 (2010). [PubMed: 20820579]
23. Low J, Yu J, Jaroniec M, Wageh S & Al-Ghamdi AA Heterojunction photocatalysts. Adv. Mater 29, 1601694 (2017).
24. Richards JJ, Whittle CL, Shao G & Pozzo LD Correlating structure and photocurrent for composite semiconducting nanoparticles with contrast variation small-angle neutron scattering and photoconductive atomic force microscopy. ACS Nano 8, 4313–4324 (2014). [PubMed: 24707810]
25. Wang L et al. Organic polymer dots as photocatalysts for visible light-driven hydrogen generation. Angew. Chem. Int. Ed. Engl 55, 12306–12310 (2016). [PubMed: 27604393]
26. Kosco J et al. The effect of residual palladium catalyst contamination on the photocatalytic hydrogen evolution activity of conjugated polymers. Adv. Energy Mater 8, 1802181 (2018).
27. Liu A, Tai C-W, Holá K & Tian H Hollow polymer dots: nature-mimicking architecture for efficient photocatalytic hydrogen evolution reaction. J. Mater. Chem. *A* 7, 4797–4803 (2019).
28. Staff RH, Landfester K & Crespy D in Hierarchical Macromolecular Structures: 60 Years after the Staudinger Nobel Prize II (ed. Percec V) 329–344 (Springer, 2013).
29. Cha H et al. Suppression of recombination losses in polymer:nonfullerene acceptor organic solar cells due to aggregation dependence of acceptor electron affinity. Adv. Energy Mater 9, 1901254 (2019).
30. Schwarz KN, Farley SB, Smith TA & Ghiggino KP Charge generation and morphology in P3HT:PCBM nanoparticles prepared by mini-emulsion and reprecipitation methods. Nanoscale 7, 19899–19904 (2015). [PubMed: 26567986]
31. Ulum S et al. Determining the structural motif of P3HT:PCBM nanoparticulate organic photovoltaic devices. Sol. Energy Mater. Sol. Cells 110, 43–48 (2013).
32. Holmes NP et al. Nano-domain behaviour in P3HT:PCBM nanoparticles, relating material properties to morphological changes. Sol. Energy Mater. Sol. Cells 117, 437–445 (2013).
33. Ge X et al. Four reversible and reconfigurable structures for three-phase emulsions: extended morphologies and applications. Sci. Rep 7, 42738 (2017). [PubMed: 28198444]
34. Subianto S et al. Sulfonated thiophene derivative stabilized aqueous poly(3-hexylthiophene):phenyl-C_{61} -butyric acid methyl ester nanoparticle dispersion for organic solar cell applications. ACS Appl. Mater. Interfaces 10, 44116–44125 (2018). [PubMed: 30474957]
35. Baran D et al. Robust nonfullerene solar cells approaching unity external quantum efficiency enabled by suppression of geminate recombination. Nat. Commun 9, 2059 (2018). [PubMed: 29802311]

36. Holliday S Synthesis and Characterisation of Non-Fullerene Electron Acceptors for Organic Photovoltaics 63–85 (Springer, 2018).
37. Huang L et al. Vertical stratification engineering for organic bulk-heterojunction devices. ACS Nano 12, 4440–4452 (2018). [PubMed: 29678114]
38. Holliday S et al. High-efficiency and air-stable P3HT-based polymer solar cells with a new non-fullerene acceptor. Nat. Commun 7, 11585 (2016). [PubMed: 27279376]
39. Endo H, Schwahn D & Cölfen H On the role of block copolymer additives for calcium carbonate crystallization: small angle neutron scattering investigation by applying contrast variation. J. Chem. Phys 120, 9410–9423 (2004). [PubMed: 15267881]
40. McKone JR, Marinescu SC, Brunschwig BS, Winkler JR & Gray HB Earth-abundant hydrogen evolution electrocatalysts. Chem. Sci 5, 865–878 (2014).
41. Stegbauer L, Schwinghammer K & Lotsch BV A hydrazone-based covalent organic framework for photocatalytic hydrogen production. Chem. Sci 5, 2789–2793 (2014).
42. Qureshi M & Takanabe K Insights on measuring and reporting heterogeneous photocatalysis: efficiency definitions and setup examples. Chem. Mater 29, 158–167 (2017).
43. Maeda K et al. Photocatalytic activities of graphitic carbon nitride powder for water reduction and oxidation under visible light. J. Phys. Chem C 113, 4940–4947 (2009).
44. Haselmann GM & Eder D Early-stage deactivation of platinum-loaded TiO_2 using in situ photodeposition during photocatalytic hydrogen evolution. ACS Catal. 7, 4668–4675 (2017).
45. Zhang G, Lan Z-A & Wang X Conjugated polymers: catalysts for photocatalytic hydrogen evolution. Angew. Chem. Int. Ed. Engl 55, 15712–15727 (2016). [PubMed: 27528426]
46. Pati PB et al. An experimental and theoretical study of an efficient polymer nano-photocatalyst for hydrogen evolution. Energy Environ. Sci 10, 1372–1376 (2017).
47. Zou X & Zhang Y Noble metal-free hydrogen evolution catalysts for water splitting. Chem. Soc. Rev 44, 5148–5180 (2015). [PubMed: 25886650]
48. Yu J, Low J, Xiao W, Zhou P & Jaroniec M Enhanced photocatalytic CO_2-reduction activity of anatase TiO_2 by coexposed {001} and {101} facets. J. Am. Chem. Soc 136, 8839–8842 (2014). [PubMed: 24918628]
49. Li H, Shang J, Ai Z & Zhang L Efficient visible light nitrogen fixation with BiOBr nanosheets of oxygen vacancies on the exposed {001} facets. J. Am. Chem. Soc 137, 6393–6399 (2015). [PubMed: 25874655]
50. Trasatti S The absolute electrode potential: an explanatory note (Recommendations 1986). J. Electroanal. Chem. Interfacial Electrochem 209, 417–428 (1986).

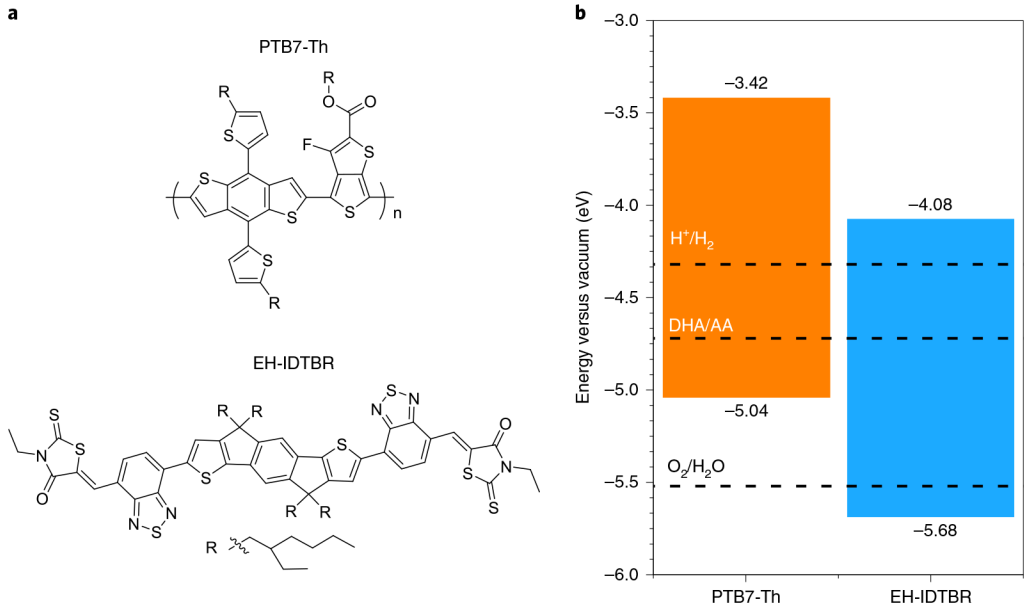

Fig. 1 |. Materials and energy levels.

a, Chemical structures of PTB7-Th and EH-IDTBR. **b**, Highest occupied and lowest unoccupied molecular orbital energy levels of PTB7-Th and EH-IDTBR compared to the proton reduction potential (H^+/H_2), water oxidation potential (O_2/H_2O) and the calculated potential of the two-hole oxidation of ascorbic acid to dehydroascorbic acid in solution (DHA/AA)[21] at pH 2 (the experimentally measured pH of 0.2 mol l^{-1} ascorbic acid). All energy levels and electrochemical potentials are expressed on the absolute electrochemical scale (0 V versus SHE = −4.44 V versus vacuum)[50].

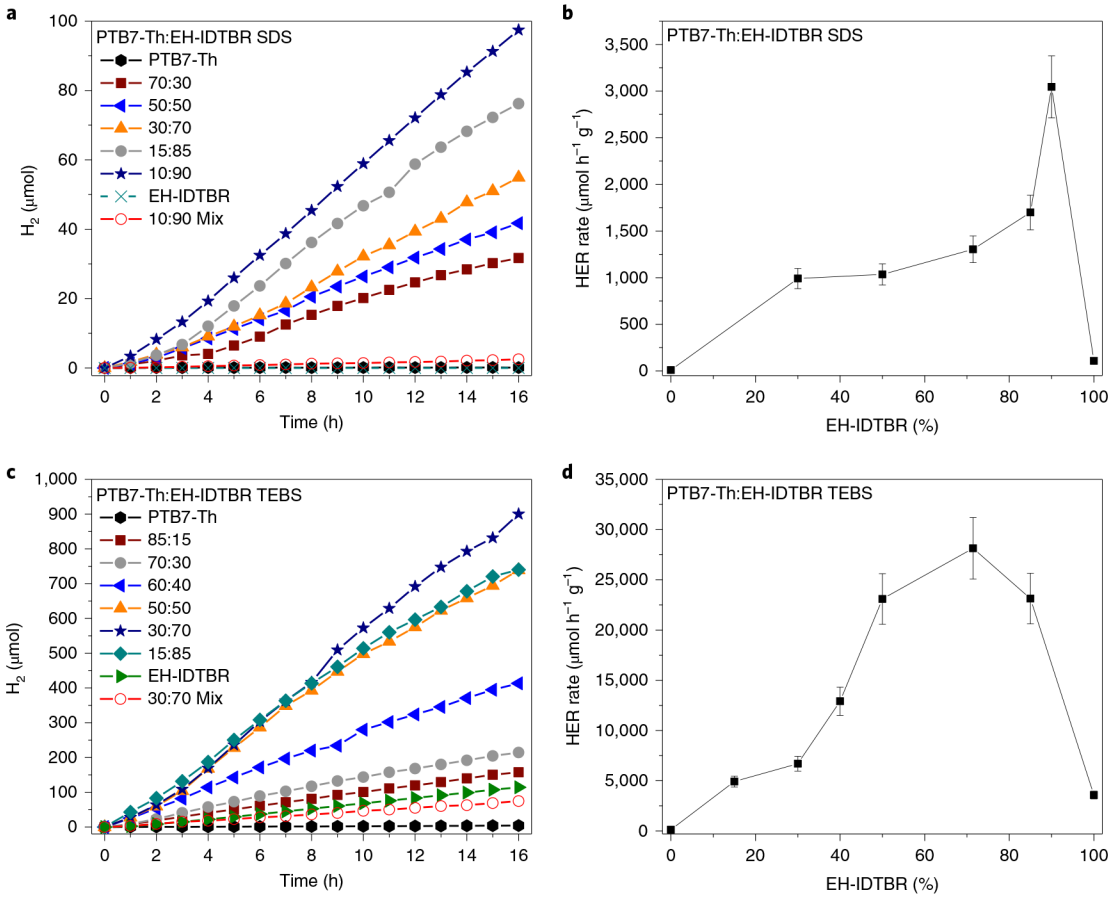

Fig. 2 |. H_2 evolution from PTB7-Th/EH-IDTBR nanoparticles.

a,**c**, H_2 evolution versus time from PTB7-Th/EH-IDTBR nanoparticles formed from a range of PTB7-Th:EH-IDTBR ratios using SDS (**a**) and TEBS (**c**) surfactant. **b**,**d**, Average H_2 evolution rates of PTB7-Th/EH-IDTBR nanoparticles formed using SDS (**b**) and TEBS (**d**) surfactant over 16 h as a function of blend composition. Conditions: 2 mg PTB7-Th/EH-IDTBR nanoparticles, 0.2 mol l^{-1} ascorbic acid (20 ml), pH 2, 5% (10 μg) Pt, 300 W Xe lamp (350 to 800 nm), 16 cm^2 reactor. Error bars were calculated as a percentage uncertainty on the basis of six repeat measurements.

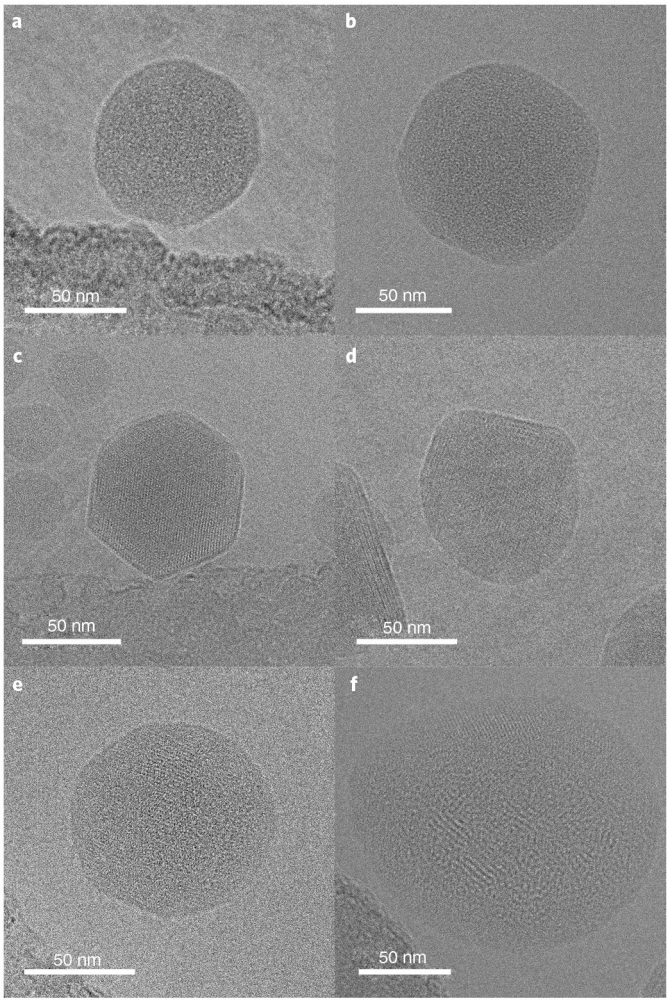

Fig. 3 |. Bright-field cryo-TEM images of nanoparticle photocatalysts showing differences in internal nanoparticle morphology.

a, PTB7-Th (SDS). **b**, PTB7-Th (TEBS). **c**, EH-IDTBR (SDS). **d**, EH-IDTBR (TEBS). **e**, PTB7-Th:EH-IDTBR 30:70 (SDS). **f**, PTB7-Th:EH-IDTBR 30:70 (TEBS). Note: the dark contrast at the bottom of images **a**,**c**,**e** arises from the carbon TEM grid. High-resolution images of **a**–**f** and detailed analysis of images **c**–**f** can be found in Supplementary Figs. 6–12.

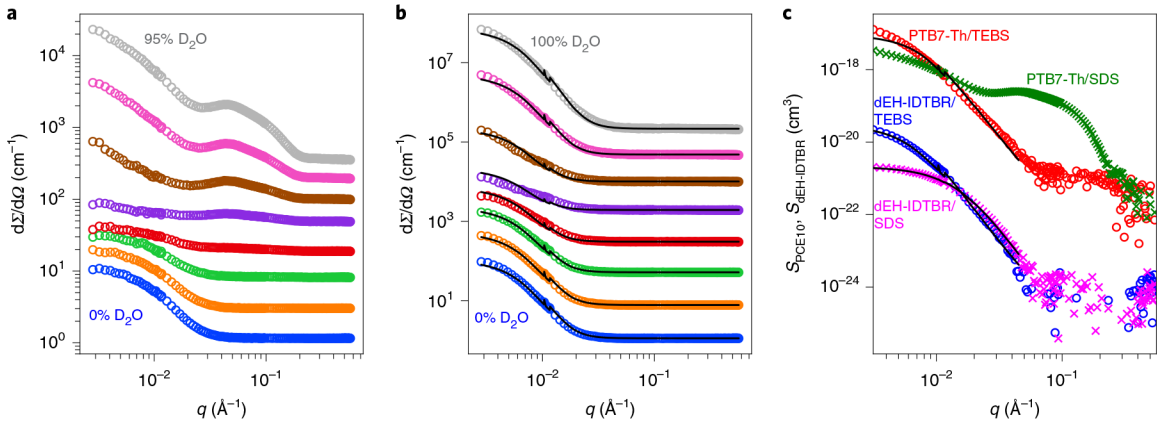

Fig. 4 |. Small-angle neutron scattering.

a–**c**, SANS (**a**,**b**) and deconstructed partial scattering functions (**c**) for PTB7-Th:dEH-IDTBR nanoparticles in H_2O/D_2O solutions with SDS (**a**) or TEBS (**b**) surfactants. In all plots, solid black lines represent a spherical form factor model fit to the data. In **a** and **b**, the curves are successively shifted by $10^{0.5}$ and $10^{0.9}$, respectively, while the upper two curves in **c** are both shifted by 10^4.

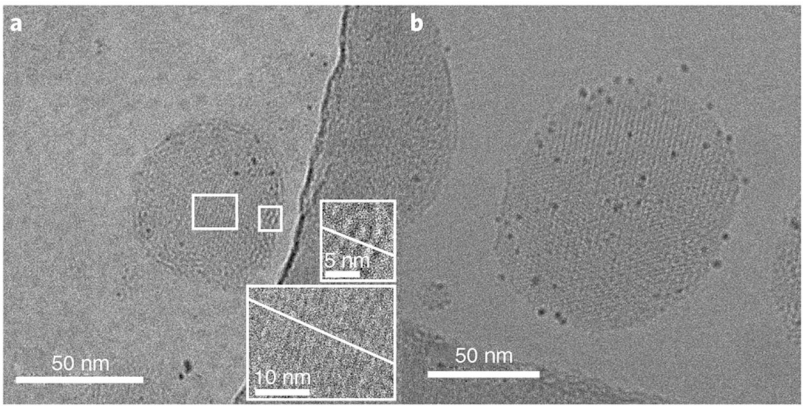

Fig. 5 |. Cryo-TEM images of NPs after deposition of Pt cocatalyst and 20 h H_2 evolution.
a, PTB7-Th:EH-IDTBR 30:70 (SDS). The upper and lower insets are magnified images of the areas in the right and left rectangles, respectively. The periodic spacings along the diagonal lines in the upper and lower insets correspond to the lamellar stacking distances of PTB7-Th (2.1 nm) and EH-IDTBR (1.6 nm), respectively (Supplementary Fig. 13)[36,37]. **b**, PTB7-Th/EH-IDTBR 30:70 (TEBS).

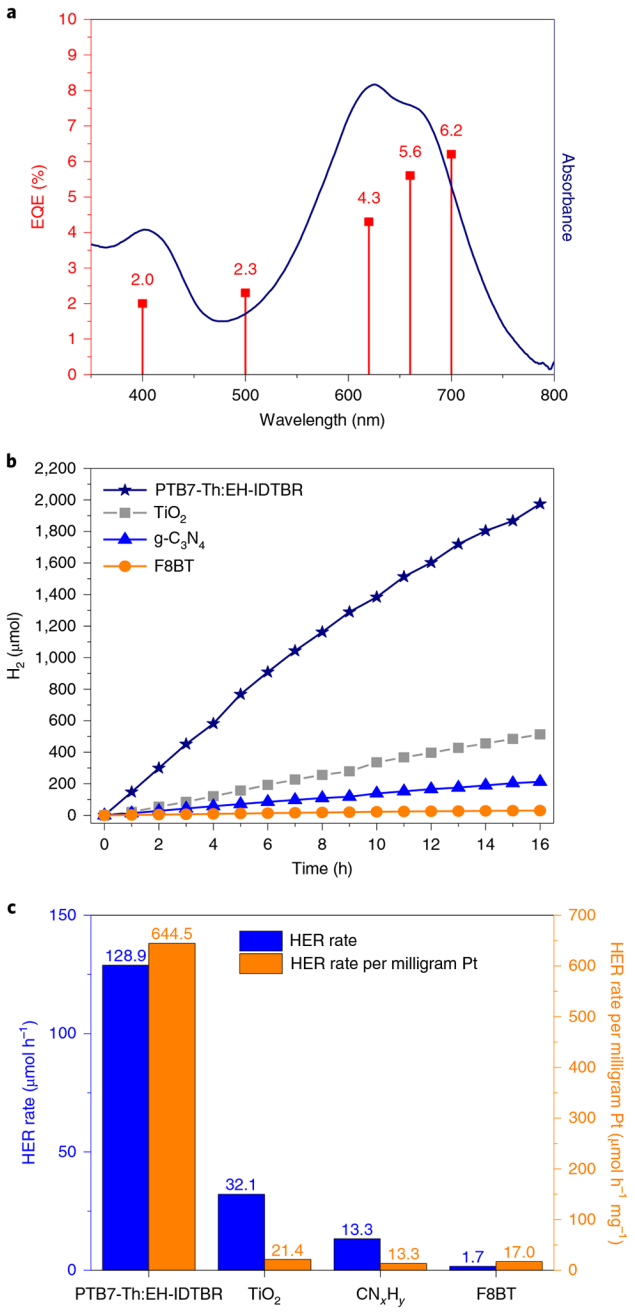

Fig. 6 |. External quantum efficiencies and performance comparison.

a, EQE at 400, 500, 620, 660 and 700 ± 10 nm and absorbance spectrum of PTB7-Th:EH-IDTBR 30:70 mass ratio (TEBS) nanoparticle photocatalysts. **b**, H_2 evolution versus time. **c**, Average H_2 evolution rates of a range of photocatalysts measured over 16 h. Conditions: PTB7-Th/EH-IDTBR: 2 mg photocatalyst, 10% Pt, 20 ml 0.2 mol l^{-1} ascorbic acid (AA). P25 TiO_2: 100 mg photocatalyst, 1.5% Pt, 20 ml 10% triethanolamine (TEOA). CN_xH_y: 100 mg photocatalyst, 1% Pt, 20 ml 10% TEOA. F8BT: 2 mg photocatalyst, 5% Pt, 20 ml 0.2

mol l^{-1} AA. Note: HER rates were higher for TiO_2 and CN_xH_y with TEOA instead of AA as the sacrificial hole scavenger. Irradiance spectra can be found in Supplementary Fig. 15.